Mesoscale variability of the summer bloom over the Northern Ross Sea Shelf: A Tale of two banks.

Josh T. Kohut[1*], Adam B. Kustka[2], Michael Hiscock[3], Phoebe Lam[4,5], Chris Measures[6], Allen Milligan[7], Angelicque White[7], Filipa Carvalho[1], Mariko Hatta[6], Bethan M. Jones[2,7], Daniel C. Ohnemus[4,8], John M. Swartz[4,9]

[1]Department of Marine and Coastal Sciences, Rutgers University, New Brunswick, NJ 08901

[2]Department of Earth and Environmental Sciences, Rutgers University, Newark, NJ 07102

[3]Office of Research and Development. United States Environmental Protection Agency. Washington D.C. 20460.

[4]Department of Marine Chemistry and Geochemistry, Woods Hole Oceanographic Institution, Woods Hole, MA 02543

[5]now at Department of Ocean Sciences, University of California, Santa Cruz, Santa Cruz, CA 95064

[6]Department of Oceanography, University of Hawaii, Honolulu, HI 96822

[7]Department of Botany and Plant Pathology, Oregon State University, Corvallis, OR 97331,

[8]now at Bigelow Laboratory for Ocean Sciences, East Boothbay, ME 04544

[9]now at Institute for Geophysics, Jackson School of Geosciences, The University of Texas at Austin, Austin, Texas 78758

*Author for correspondence email: kohut@marine.rutgers.edu

Keywords: Ross Sea, Phytoplankton, Trace Metals, Mixed Layers, light and iron limitation, bathymetry.

ABSTRACT

The importance of seasonal blooms across the Ross Sea is well documented. Multi-year satellite records indicate that there is a persistent spatial pattern in the summer bloom in the Northern Ross Sea, with more consistent biomass over the shallows of Pennell Bank compared to Mawson Bank. In 2010-2011, we deployed multiplatform technologies during a bloom that was consistent with this long-term trend. High-resolution spatiotemporal sampling focused on these two banks to highlight differences that may have influenced this observed pattern. Dissolved and particulate Fe profiles were comparable on both banks with notably similar surface water drawdowns of dissolved Fe. The surface sediments and velocity observations associated with each bank indicate a more energetic water column over Mawson Bank compared to Pennell. Consequently, the mixed layer over central Pennell Bank was more homogeneous and relatively shallow. Conversely, at Mawson Bank, we observed deeper and less homogeneous mixed layers with potentially lower vertical fluxes of iron into the euphotic zone. Based on underway Fv/Fm measurements, both Mawson Bank and Pennell Bank populations appear to be growth rate limited by iron availability. Productivity rates and biomass were elevated on central Pennell Bank compared to Mawson Bank. Additionally, estimates of the quantum yield of photosynthesis and the initial slope of the photosynthesis-irradiance response (α) were lower over Mawson Bank, indicating higher iron stress over Mawson Bank. Overall, this suggests that the vertical flux of Fe to the surface waters on Mawson Bank may have been impeded. This hypothesis is supported by the fundamental differences in the physical structure of the water columns at the two locations.

1. Introduction

Phytoplankton blooms in the Ross Sea are large (Arrigo & van Dijken, 2004), high productivity events (Arrigo & McClain, 1994) that are responsible for large quantities of carbon export (Asper & Smith, 1999). The Ross Sea continental shelf has the highest rates of net primary productivity in Antarctica (Arrigo et al. 2008a, Smith & Comiso 2008), is a major regional CO_2 sink (Arrigo et al. 2008b) and phytoplankton communities support a robust food web containing 16 species of upper trophic level predators such as penguins, cetaceans and seals (Ballard et al., 2012; Smith et al., 2014). In other regions, physical features have suggested that the spatial distribution of phytoplankton blooms and grazers may be linked to local bathymetry and/or tides (Hunt, 1998; Cotté and Simard, 2005, Vlietstra et al., 2005). Since these features are dynamic, seasonal blooms are often characterized by patchy distributions in both time and space.

In the Ross Sea there is a temporal progression in the phytoplankton composition that is potentially driven by varying physical controls on light regime and/or iron supply, although the exact contribution of each factor is debated. In the spring, strong katabatic winds push sea ice offshore and create relatively deep mixed layers. Communities in these waters are often dominated by the haptophyte *Phaeocystis antarctica*, but by early summer the polynya assemblage becomes increasingly dominated by diatoms (Arrigo et al., 1999). The springtime dominance of *P. antarctica* is consistent with its photo-physiology, which is well suited for irradiance conditions resembling those of a deep mixed layer with a dynamic light regime (Kropuenske et al., 2009). As the season progresses, the water column becomes more stratified, leading to conditions suitable for the photo-physiology of diatoms such as *Fragilariopsis cylindricus* (Kropuenske et al., 2009). Therefore, the spring to summer shifts in community assemblage from *P. antarctica* to diatoms may be related to changes in Mixed Layer Depth (MLD) and light regime. However, concurrent changes in dissolved iron (Fe) potentially confound this relationship. As the polynya first opens, surface water dissolved Fe concentrations can be as high as ~4 nM (Sedwick et al., 2000). These springtime dissolved Fe concentrations are rapidly drawn down by *P. antarctica* blooms (Sedwick et al., 2011), leading to concentrations that typically remain low throughout the summer. The extent to which these lower Fe concentrations lead to preferential growth of diatoms is not clear. On one hand, some *P. antarctica* populations in the Antarctic Circumpolar Current require higher dissolved Fe concentrations for growth compared to co-occurring diatoms (Coale et al., 2003), and incubation experiments in the Ross Sea have revealed a preferential stimulation of *P. antarctica* by added Fe (Bertrand et al., 2007). However, other field observations and deck incubation results suggest low Fe conditions tend to favor *P. antarctica* over diatoms (Sedwick et al., 2000). Culture experiments demonstrating that species grown under low light have elevated Fe requirements, presumably due to the increased need for Fe-expensive photosynthetic electron transport chains (Sunda and Huntsman, 1997), which may further complicate our understanding of iron and light limitation in the Southern Ocean.

The interplay between micronutrient sources, water column stability, shelf circulation, and local topographic features drives a persistent response in the summer bloom over the northern Ross Sea shelf. This is a critical region for both the exchange of dense bottom water masses that move down the slope and eventually form dense Antarctic Bottom Water (AABW, Gordon et al., 2009) and the injection of warm

Circumpolar Deep Water (CDW) that comes from the mid-depths of the Southern Ocean. The most energetic process that likely contributes to the mixing and advection of these water masses is tides. The tides of the Ross Sea are predominantly diurnal with higher amplitudes over the shallow banks and along the shelf break (Robertson, 2005; Whithworth and Orsi, 2006; Padman et al., 2009). The tides interact with the varying topography and the background flow over the northern Ross Shelf to mix and modify the water masses, likely influencing phytoplankton production in the summer bloom through varying water column stability and delivery of micronutrients to the euphotic zone (Arrigo & Van Dijken, 2004; Dinniman et al., 2003; Gordon et al., 2009).

Satellite based ocean color time series highlight a persistent spatial pattern of the biomass along a transect spanning the outer Ross Shelf including Mawson Bank (MB) and Pennell Bank (PB). NASA Moderate Resolution Imaging Spectroradiometer Aqua (MODIS-A) mapped, 8-day, 9km, standard chl *a* estimates (mg m^{-3}) from the 2013 MODIS-A Reprocessing 2013.1 were downloaded from http://oceandata.sci.gsfc.nasa.gov for 1998-2014. Chlorophyll composites were generated for January 1 – February 25 of each year along a 5 pixel wide (~46 km) swaths centered on a transect that includes PB and MB (Figures 1 and 2). While there is significant year to year variability in chlorophyll across the region, possibly due to differences in physical forcing and timing of ice melt, there has been a relatively persistent pattern across these banks with higher chlorophyll concentrations over central PB and the eastern slope of MB (Figure 2c). The time mean of this section over all years sampled clearly shows a peak in biomass over PB with a secondary peak over the eastern slope of MB (Figure 2d).

During the austral summer of 2011, the spatial pattern of the summer bloom over central PB and the eastern slope of MB matched this multi-year mean pattern (Figure 2a). The consistency of the spatial pattern between the summer 2011 bloom and the mean pattern observed over the multi-year satellite record motivates this study. We describe the characteristics of each bank as they relate to the relative distribution of biomass associated with the 2011 summer bloom over the northern Ross Sea Shelf as a proxy for conditions that likely drive the persistent pattern observed in the satellite climatology. We integrate physical, biological and chemical measures sampled across coincident ship and AUV based surveys to determine the conditions that support the observed spatial pattern across the two banks. Section 2 describes the various methods used in our analysis. Results are presented in Section 3. We conclude with a discussion of the similarities and differences between the coupled physical, biological, and chemical processes that drive the persistent pattern in the spatial distribution of the summer bloom over the Northern Ross Sea in sections 4 and 5.

2. Methods

2.1 Cruise Transect and Underway Measurements

***2.1.1 Hydrography*:** A ship survey was completed aboard the *RVIB Nathaniel B. Palmer* (NBP). The ship left McMurdo Station on January 19th, 2011 on a 26 day cruise focused primarily on the Northern Shelf across PB and MB (Figure 1). Throughout the cruise, underway measurements of temperature and salinity were taken every second with the NBP thermosalinograph at an intake depth of 6.7 m below the surface. These data were subsampled every 10 seconds along the ship's track. Vertical profiles of velocity were sampled by a ship mounted downward looking 150 KHz Acoustic Doppler Current Profiler (ADCP). These shipboard data were processed with the University of Hawaii Data Acquisition System (UHDAS) software. Five minute ensembles were collected with a vertical bin resolution of 8 meters. Raw depth averaged and depth dependent data were detided using the predicted barotropic tide derived from Ross Sea sub-region of the Oregon Tidal Prediction System (Figure 4; Erofeeva et al., 2005).

In addition to the underway data, the ship survey completed 79 stations (Figure 1). Over the course of the cruise the ship made 8 repeat transects across PB and MB (Figure 1). Along this cross section of the banks we sampled 9 stations; 5 over PB, 3 over MB, and one over Joides Basin (Figure 1). At each station there were at least 3 CTD casts with a maximum of 8 casts sampled at the station over the 400 m isobath along the western slope of PB. At each station, at least one full water column profile of the ship's CTD rosette was completed. The Sea-Bird CTD mounted on the rosette was calibrated before and after the cruise. Our analysis will focus in on a single along bank section from off the shelf to the southern end of PB and the 8 repeat cross-sections across PB, Joides Basin, and MB (Figure 1).

***2.1.2 Dissolved Trace Metals*:** Over 180 samples were collected for trace metal determinations at 15 of the 79 stations using a custom-built trace metal clean rosette consisting of an epoxy painted Al rosette frame containing 12 x 12L GO-FLO bottles (Measures et al., 2008). Filtered seawater samples (0.45 µm pore size, pre-acid washed, 47 mm polysulphone filters Pall Supor 450 P/N 60173) were collected and drawn into acid pre-washed 125 ml polymethylpentene bottles after three sample rinses; sample bottles were stored in polyethylene bags in the dark at room temperature before the determination, which was usually within 24 hours of collection. Also, duplicate samples were collected and drawn into pre-acid leached 125 mL HDPE bottles after three sample rinse for shore-based determination of dissolved Fe by Inductively Coupled Plasma Mass Spectrometry (ICP-MS), Milne et al. (2010), in order to obtain the shipboard blank values.

As described in Hatta et al. (this volume), dissolved Fe was determined in the filtered, acidified, microwave-treated subsamples using flow injection analysis (FIA) methods of Measures et al. (1995) for dFe determinations. The detection limit and the precision of dFe determination was approximately 0.12 nM and 3.1% at 1.3 nM. Shipboard data sets have been compared with the ICP-MS data to calculate and correct for the shipboard FIA system blank for dFe.

2.1.3 Particulate Trace Metals: Particulate trace metal concentrations were determined on particles collected by in-situ filtration as described in Hatta et al., (this volume). Briefly, size-fractionated particles (>51 µm, 0.8 - 51 µm) were collected by in-situ filtration using modified dual-flow McLane WTS pumps (Ohnemus and Lam, 2015). The 0.8 - 51 µm size fraction was used to determine the total and leachable concentrations of particulate trace metals. Total digestions were effected with the Piranha method, which completely dissolves the filter and all lithogenic particles (Ohnemus et al., 2014; Ohnemus and Lam, 2015). Leachable concentrations of particulate trace metals were determined using a 1M hydrochloric acid (HCl) leach at room temperature for 24 hours. This cold HCl leach is more aggressive than other commonly used weak acid leaches (e.g., Berger et al., 2008), but has the advantage of having been tested on a variety of iron bearing minerals: it has been shown to extract Fe from poorly crystalline Fe(III) oxyhydroxides and a small fraction of some phyllosilicates, but not crystalline Fe(III) oxides (Raiswell et al., 1994). Total digest and leach solutions were run at the WHOI Plasma facility on a Thermo Element2 HR ICP-MS using a quartz spray chamber introduction system (Ohnemus et al., 2014; Hatta et al., this volume).

2.1.4 Surface sediments grain size analysis: Surface sediments were collected using a Smith McIntyre Grab at stations along the southern across-bank section at the 400 m isobaths on the western and eastern flanks of PB and MB (stations 71-MB West, 35-MB East, 41-PB West, 28-PB East), at the top of each bank around 280 m depth (stations 70-Central MB, 26- Central PB), and at 595 m water depth in the Joides Basin in between the two banks (station 34-JB). Additional samples were collected at select stations offshore and inshore of the main section (Figure 1). Sediment subsamples were transferred to 50ml centrifuge tubes and spun down on-board to remove most pore waters, and then frozen for transport.

Grain size distributions were determined for surface sediments along the main across-bank section. Sediments were thawed in the laboratory, and subsamples were transferred to a 15mL centrifuge tube and shaken vigorously in water to disperse aggregates, and sieved to remove gravel pieces >2 mm. Grain size distribution for sediments <2 mm was determined on a Beckman Coulter LS13320 Laser Diffraction Particle Size Analyzer at the WHOI Coastal Research Facility. The LS13320 determines the volumetric size distribution from 0.017 μm to 2000 μm. Samples were introduced into the Particle Size Analyzer in an aqueous stream, and sediment concentration was adjusted to reach an obscuration rate between 10-20%. Volume percentages were binned into clay (<4 μm), silt (4-63 μm), and sand (63-2000 μm) size classes (Wentworth, 1922). Broad characteristics of sediment samples off of the main across-bank section were grouped into qualitative sediment classes on the basis of their textural similarities to the sediments for which the grain size distributions were determined (Figure 1).

***2.1.5 Biological sampling*:** Measurements of photosynthetically active radiation (PAR) were taken continuously with a BSI QSR-240 sensor positioned on the mast. Underway parameters, including particulate organic carbon (POC, estimated from beam attenuation) and variable to maximum fluorescence (F_v/F_m), were measured from water collected 6.7 m below the surface, from the ship's underway seawater system. For attenuation and particulate carbon, this source water was routed through a Vortex debubbler and a valve control device that automatically diverted the inflow to a PALL Supor 0.2 μm membrane filter for the first 10 minutes of every hour prior to passing through a Wetlabs hyperspectral absorbance and attenuation (ac-s) meter. For the remaining 50 minutes of each hour, the valve control device routed water from the debubbler directly to the ac-s. Particulate beam attenuation spectra were corrected as per Slade et al. (2010). All raw data were binned to 1-min intervals, the dissolved attenuation signal [$c_d(\lambda)$] was subtracted from the unfiltered attenuation signal [$c_t(\lambda)$] to obtain particulate spectra [$c_p(\lambda)$] which were then corrected for variations in particle beam attenuation resulting from residual temperature differences between filtered and unfiltered spectra (see Slade et al. (2010)). For reference, at 660 nm the magnitude of dissolved attenuation values were 0.0220 ± 0.0138 m^{-1}. Discrete samples (triplicate samples collected at 6 discrete times, n=18) were collected from the outflow of the ac-s for calibration of $c_p(660)$ to particulate organic carbon (POC) as measured by high temperature combustion of particulate matter filtered onto glass fiber filters. The POC to c_p slope for this data set is 345 mg C m^{-2} with an intercept of 1.7 mg C m^{-3}; these values were used to transform the full corrected $c_p(660)$ dataset to POC values. This slope is consistent with that reported by Cetinic et al. (2012) for diatom dominated communities within the mixed layer (369 ± 23 mg C m^{-2}) and with the global analysis of Gardner et al. (2006) which report a slope of 381 ± 3 mg C m^{-2} and an intercept of 9.4 ± 0.6 mg C m^{-3}.

2.1.6 Productivity: Photosynthesis-irradiance experiments were conducted using a ^{14}C-radiotracer method. Samples were collected from 5 m using the trace metal clean rosette or by TMC pumping of surface water (Vink et al., 2000). Water samples were processed in a flow hood and all plasticware was acid washed with 10% trace metal grade HCl (Martin et al., 1991). Incubation chambers consisted of two photosynthetrons (OHPT Inc. Delaware, USA); irradiance was controlled with both copper sulfate and neutral density filters with incubation light levels ranging from 0 - 300 µmol photons m^{-2} s^{-1}. Incubation temperatures were maintained at a constant 0°C via circulating water baths filled with a 90% glycerol solution. At each station 50µL of a 0.2 mCi ^{14}C-HCO_3^- L^{-1} stock was added to 80 mL of sample to achieve a final ^{14}C-concentration of125 pCi mL^{-1}. Following the addition, the sample was gently inverted and 100 µL placed into a scintillation vial containing 1 mL of 0.2 µm filtered seawater (FSW) and 100µL of β-phenethylamine to determine the specific activity. The remaining sample was dispensed among 15 polyethylene scintillation vials with a final volume of 5 mL per vial. Samples were incubated for 24 h (and therefore reflect net primary production rather than gross production which is often seen in shorter incubations (Halsey et al., 2011) and acidified with 250 µL of 10% hydrochloric acid in a fume hood for 8-12 h, after which 19 mL of

Ecolume scintillation fluid were added. Radioactivity was measured on Tri-Carb liquid scintillation counter after 24 h and again after 1 week. For each experiment, duplicate vials were wrapped with aluminum foil before incubation and the corresponding dark ^{14}C-fixation was subtracted from the light values. Primary productivity was calculated by multiplying the percent of carbon labeled by the total carbon available for photosynthesis (e.g. total alkalinity calculated from SST and salinity measured at each station as per Lee et al. (2006) and dividing by incubation time. Rates were also normalized to the concentration of fluorometric derived chlorophyll a determined by extraction in 90% methanol (Strickland and Parsons, 1972).

The results of each P–E experiment were fit to a hyperbolic tangent model of Jassby and Platt (1976) using a least-squares non-linear regression in Matlab™ in order to estimate the maximal photosynthetic rate (P^{max} and P_B^{max}) and the light utilization coefficient (α and α_B) with the latter terms calculated after normalization of rates to chlorophyll. The light-saturation index E_K is the quotient of P_B^{MAX} and α_B. Particulate absorption spectra were measured for each incubation as per the quantitative filter pad method described in Mitchell (1990) and Kishino et al. (1985). Briefly, total absorption was measured, methanol was subsequently used to extract pigments from the filtered sample, and detrital absorption was measured. The difference between the two spectra represents lipid-soluble absorption by phytoplankton pigments (a_p (λ)). The mean spectrally weighted $\bar{a}_p$ (m^{-1}) was then calculated as in Hiscock et al., (2008) using the scalar irradiance of the photosynthetron light banks ($E(\lambda)$). Photosynthetically usable radiation for each light level was then calculated as PAR multiplied by $\bar{a}_p$. The initial slope of PUR relative to ^{14}C fixation, again determined via least-squares non-linear regression in Matlab™ is an estimate of the quantum yield of carbon uptake (ϕ). All parameters are shown in Table 3. Productivity rates were integrated over the mixed layer using measured P_{max}, α and K_{PAR} values and mean daily integrated surface PAR.

2.1.7 Phytoplankton Community Composition: Eukaryotic plankton community structure was investigated using a quantitative high throughput sequence approach targeting the hypervariable V7-9 regions of 18S eukaryotic ribosomal DNA with the Pacific BioSciences SMRT (single molecule real time) sequencing platform. Samples taken from station 7 (Central PB), station 14 (at the shelf break), station 24 (Joides Basin), station 48 (northern PB) and station 70 (Central MB) were extracted and analyzed. Technical details of sample collection, DNA extraction and subsequent processing, are presented in Jones and Kustka (submitted). Sequences were clustered into Operational Taxonomic Units (OTUs) at 98% similarity. For the purposes of this study, data derived from clades that could be reasonably assigned to the phytoplankton were analyzed since this group is directly responsible for primary productivity and is directly influenced by iron and light availability. Therefore, metazoan sequences (e.g. sequences from copepods, krill) and those derived from protozoan grazers were omitted. Additionally, those from dinoflagellates and *Pyramimonas*-like organisms were also removed from downstream analyses because many are not strictly photosynthetic. After this, rare OTUs (comprising less than 1% of the total OTU copies within all stations) were omitted since their importance from an ecological perspective is not obvious. It is also noteworthy that the copy number of 18S rDNA is not directly translatable to cell numbers; this is particularly the case for dinoflagellates, where copy numbers can range from hundreds to thousands of copies per cell depending on the species (Zhu et al. 2005);

relatively rare dinoflagellates can result in disproportionate contributions to community structure. While dinoflagellates were present in the unfiltered dataset, there was very scant evidence of this group from shipboard microscopic examinations (Angelicque White, unpub. data). Relative abundances of the different OTUs were compared.

A single sample was collected for each station location, while other samples from complementary incubation experiments were collected from replicate cubitainers. The coefficients of variation for the relative abundances of moderately abundant OTUs (15% or greater) from samples collected from replicate treatments presented in Kustka et al. (2015b) averaged 0.16 (±0.14). This provides an indication of the general reproducibility of our analyses of relative abundances of community composition.

2.2 Autonomous Glider Deployments

Two gliders manufactured by Teledyne Webb Research were deployed in the Ross Sea during the cruise. The buoyancy-driven propulsion of the glider AUV affords high efficiency and deployment endurance (Schofield et al., 2007). Throughout the missions the gliders moved in a sawtooth pattern between 3 m below the surface to 100 m deep. Each glider was equipped with a sensor suite that characterized the ecosystem's physical structure (Conductivity, Temperature, Depth), *in situ* phytoplankton fluorescence and optical backscatter. One glider deployed on February 1, 2011 completed a 9 day mission back and forth across PB. On February 4, 2011 a second shallow glider was deployed near the eastern slope of MB completing a 4 day mission to the west across the bank (Figure 1). The CTD and optical resolution was 0.25m in the vertical and approximately 250m in the horizontal.

2.3 Mixed Layer Depth (MLD) Estimation

For this analysis we chose a MLD definition that best linked the physical structure with the biological responses. Based on a recent analysis of hydrographic data sampled in the Ross Sea, Amundsen Sea, and along the Western Antarctic Peninsula, the definition that showed the most ecological relevance, i.e., the one where the physics best match the biology (using a linear regression fit), was using buoyancy frequency or Brunt-Väisälä frequency (N^2; Equation 1, Carvalho et al., in Prep). For each profile, MLD was determined by finding the depth of the maximum water column buoyancy frequency – max (N^2), as defined by

$$\max(N^2) = \max\left[-\frac{g}{\rho}\frac{\partial\rho}{\partial z}\right] \qquad (1)$$

The determination of MLD is based on the principle that there is a near-surface layer characterized by quasi-homogeneous properties and where the standard deviation of the property within this layer is close to zero. Below the MLD, the variance of the property should increase rapidly above its vertical mean. For each profile, a quality index (Equation 2) by Lorbacher et al. (2006) was used to quantify the uncertainty in the MLD estimate. Using

$$QI = 1 - \frac{rmsd(\rho_k - \bar{\rho}_k)|_{(H_1, H_D)}}{rmsd(\rho_k - \bar{\rho}_k)|_{(H_1, 1.5\times H_D)}}, \qquad (2)$$

where rmsd( ) denotes the standard deviation from the vertical mean $\bar{\rho}$ from H_1, the first layer near the surface, to a depth D or 1.5xD (where D is the depth of the mixed layer). This index evaluates the certainty in the MLD estimate, where values between 0.8 and 1 represent MLD that were determined with certainty (QI>0.8), values between 0.5 and 0.8 represent MLDs determined with uncertainty (0.5<QI<0.8), and values below 0.5 for MLD estimates that could not be determined (QI<0.5). This index does not take into account how strong that inflection is, i.e. how stratified the water column is; just that there is a homogeneous layer present and the MLD calculated is close to the lower boundary of that vertically uniform layer.

3. Results

3.1 Physical conditions

Repeated survey transects across PB and MB and the intervening Joides Basin highlights the similarities and differences between the oceanographic conditions associated with each bank. Along the western slope of both banks a predominantly barotropic flow delivers deep offshore waters onto the shelf (Figure 3, from Kohut et al., 2013). Differences in the bathymetry of the each bank impact the fate of these intrusions as the flow wraps around each bank (Kohut et al., 2013). Beneath our central transect, MB is characterized as a relatively narrow feature approximately 300 meters deep at its shallowest. Pennell is a much broader and slightly shallower bank with an asymmetric profile. West of the 250 m deep peak, the bank has a much steeper slope than the more gentle slope to the east. The most concentrated MCDW signals are seen near Joides Basin and the western slopes of PB and MB. The deep High Salinity Shelf Water (HSSW) is only observed in stations at least 400 m deep. The mean cross section based on all the casts taken at each station shows the significant variation in water column properties across the complicated topography (Figure 4). There is a distinct surface layer of warmer fresher water across the entire section with slightly fresher water over the western slopes of the banks. At depths greater than ~ 80 m there is significant variability in the distribution of the deeper water masses. In Joides Basin there is a thick layer of dense shelf water reaching up from the bottom to a depth of about 250 m. Above the western slope of PB, there is a distinct slug of warmer, lower oxygenated MCDW at depths between 180 and 250 m, centered over the 400 m isobath. While there is evidence of a similar slug of MCDW over the western slope of MB, its potential temperature and oxygen signals are more dilute and spread over a wider range of depths. West of MB the mid water densities consistent with MCDW (Orsi and Wiederwohl, 2009) are more spread vertically throughout the water column, and unlike PB where the MCDW is concentrated over the western slope, the neutral densities that help delineate MCDW extend eastward across the bank.

The hydrography and chlorophyll fluorescence within the upper 100 m were simultaneously sampled over 2 glider missions, one across each bank (Figure 1 and 5). Over PB, the thermal stratification sampled across the glider section increases in the upper 100 m of the water column proceeding east from Joides Basin toward the peak of PB (Figure 5, right column). The transect across MB highlights a region of thermally stratified water over the eastern slope punctuated by a well-mixed water column over the shallows of the bank itself (Figure 5, left column). For both banks the highest chlorophyll fluorescence is observed in surface waters above the stronger thermal stratification. Over PB this occurs over the center of the bank and, over MB, the stronger stratification and highest fluorescence is seen over the deeper waters of the eastern slope of the bank. This observed pattern is consistent with both the multi-year satellite record and the 2011 MODIS snapshot taken during our survey (Figure 2).

MLDs measured at repeat stations over central PB were persistent over time and were all between 29 and 55 meters (Figure 6). Additionally, the high quality index (QI) values for 4 of the 5 stations indicate that these MLD estimates are defined with certainty. Conversely over MB, the QIs for the estimated MLDs were generally lower, with values between 0.40 and 0.84. Two of the 6 repeat stations have QI values below 0.5 indicating that a MLD could not be determined. The MLDs that could be determined were mostly done so with uncertainty ($0.5 < QI < 0.8$). The QIs for these MLDs all fell between 0.57 and 0.6. The only MLD defined over central MB with certainty (QI = 0.84) was 76m deep on February 12, Station 78. Coincident profiles of Chl-*a* fluorescence at the PB repeat stations correlate well with the estimated MLDs with peak values above the derived MLD. The lower Chl-a concentrations observed at the MB repeat station were spread more vertically and less correlated with the estimated MLDs when an estimate could be made (Figure 6).

3.2. Dissolved and Particulate metals

The distribution of dissolved Fe (dFe) shows increased concentrations at depth at both MB (up to ~ 0.28 nM) and at repeat stations on PB (~0.22 - 0.36 nM; Figure 7a). Upper water column concentrations were generally low (~0.15 nM) with the exception of two elevated surface water observations for station 61 (discussed below). Total and leachable particulate Fe (pFe) concentrations were uniformly low at the surface (~0.1 nM) and increased strongly with depth at all stations (Figure 7b; Hatta et al., this volume). Near bottom concentrations of total and leachable pFe were highest over MB compared to PB. The proportion of total pFe that was leachable (%leachable pFe) was either constant or decreased with depth.

3.3 Seafloor Sediments

The surface sediment grain size distributions for sediments <2 mm along the main across-bank section are indicated in Table 1. Sediment characteristics followed a similar pattern from west to east across each bank, albeit with different characteristics relative to the topography of each bank. Surface sediments from the western flanks of both MB and PB (MB West, PB West) were characterized by >70% sand, but also contained rocks and abundant gravel pieces >2 mm that were sieved out before being analyzed for grain size distribution (not shown). The sediments at the top of MB (70-Central MB) had abundant consolidated clay and did not have an analogue in any of the sediments sampled on PB. The sediments underlying the higher productivity zones on the eastern flank of MB (35-MB East) and the top of PB (26-Central PB) were both characterized by >70% sand, but less gravel or rocks compared to the sediments on the western flanks. Finally, the sediments to the east of the high productivity regions in the Joides Basin (34-TR) and the eastern flank of PB (28-PB East) were characterized by >70% silt (diatom ooze).

Sediments off the main across-bank section were not analyzed for particle size distribution, but were classified on the basis of their textural similarities to the sediments on the main section (Figure 1). In general, the sediments in the offshore direction toward the shelf-break were dominated by larger size classes (sand, gravel), whereas the sediments in the inshore direction toward the Antarctic continent were dominated by silt. The general trend observed was thus a progression from a dominance of large to small sediment size classes across the banks from west to east, and along the banks from offshore to inshore.

The western flank stations associated with each bank were the locations of the highest depth averaged currents (Figure 3). The wide range in size distribution for sediments at these stations is consistent with strong currents on the western flanks winnowing away fine sediments, exposing the poorly sorted mixture of sediment that reflects the underlying glacial till of the Ross Shelf (Anderson et al., 1984).

In contrast, the sediments with high percentage of silt (diatom ooze) indicate relatively quiescent physical conditions that allow for the accumulation of these fine sediments. Indeed, the eastern flank of PB (28-PB East) had the lowest depth averaged currents over the across-bank section (Figure 3). The Joides Basin sample was taken close to where the depth-averaged current was zero, shifting from predominantly offshelf to onshelf (Figure 3, Figure 11, Kohut et al., 2013), and its deeper location may function as a local deposition center for winnowed sediments surrounding it.

3.4. Phytoplankton biomass and production

Surface water POC, an estimate of planktonic biomass, had elevated concentrations along portions of PB, while MB had concentrations lower than PB but slightly greater than along Joides Trough (Figure 2b). These features are generally consistent with the multi-season trends in biomass, as approximated by MODIS-derived chlorophyll *a* data (Figure 2). However, while biomass levels were lower on MB, Fv/Fm values obtained at CPB and MB were uniformly low (0.294± 0.024; n= 4 and 0.266± 0.027; n=2, respectively, Table 2). These low values are consistent with Fe-limited growth across the region and corroborated by Fe addition incubations (Kustka et al. 2015a).

Biomass normalized maximum productivity values ranged from 1.5 - 8.4 g C g chl a^{-1} h^{-1} across the study area, and values for α (the initial slope of the photosynthesis-irradiance curve, [mg C m^{-3} d^{-1} (μmol photons m^{-2} $s^{-1})^{-1}$] ranged from 0.3-5.5 (Table 3) with the highest values measured over PB (station 64, see Fig. 2B). This trend holds for α_B: values ranged from 0.047-0.074 over MB and 0.04-0.12 over PB [g C g chl^{-1} h^{-1} (μmol photons m^{-2} $s^{-1})^{-1}$]. Similarly, the quantum yield, ϕ, measured in deckboard incubations was also elevated over PB, reaching values of 0.06-0.07 mol C mol $photons^{-1}$ over central PB relative to 0.013-0.022 over MB. Productivity rates integrated over the mixed layer were most pronounced in the PB region (~up to 6.4 g C m^{-2} d^{-1}) compared to the lower values observed at MB (~0.6 - 1.1 g C m^{-2} d^{-1}) and other stations (Table 3). We hypothesize that these changes in physiology, e.g. enhanced ϕ, α_B and, α over PB reflect enhanced Fe fluxes to this region relative to MB.

We note that integrated production is sensitive to the MLD definition used. As a result the absolute productivity values calculated in this study and those calculated in an earlier study, from the same data set, differed (Kustka et al., 2015b). However, the trends between the banks and between stations around PB itself are consistent.

3.5 Phytoplankton Community Composition

Relative abundances of 18S rDNA corresponding to various genera of phytoplankton are given in Figure 8. *Fragilariopsis* 18S rDNA abundances were very similar at both station 7 (Central PB) and station 70 (MB; 5 and 6% of the total phototrophs, respectively). Also, the relative abundance of *Phaeocystis* rDNA was also similar and very low at these stations, with abundances less than or equal to 1%, consistent with microscopic observations (unpublished). Two distinct clades of *Chaeotoceros*, referred to as clades 1 and 2, collectively dominated sequences obtained from PB (55%) but had a minor contribution (3.2%) at MB, similar to that observed for the shelf-break station 14. The most striking difference observed between both PB and MB was the dominance of a "*Chaeotoceros*-like" clade, (95% similarity to *Chaetoceros* species within the NCBI-nr database) which comprised 10% and 62% of the sequences obtained from these two stations, respectively.

4. Discussion

Over the northern Ross Sea Shelf a multi-year satellite record highlights a persistent pattern in the distribution of the summer bloom over MB and PB. While there are similarities between both banks, there are critical differences in local physical oceanography and biogeochemistry associated with each bank that persistently support greater phytoplankton biomass over central PB compared to central MB.

The MLDs estimated over central PB were well defined and persistent with an average depth shallower than 40 meters. The relatively weaker currents due to weaker tides compared to those over MB likely leads to the more persistent, homogeneous and shallower MLDs (Figure 6). Conversely, MB is characterized by stronger tidal currents and weaker surface stratification (Figures 5 and 6). Under these conditions, MLDs were defined with greater uncertainty due to a more gradual density gradient in the upper 100 m of the water column, lacking the homogenous surface layer that persisted over PB.

The predominance of sandy sediments over MB are consistent with the stronger tidal currents there and are not expected to be strong sources of reduced Mn or Fe because of higher oxygen penetration into these porous sediments. Silty sediments, as were found over some stations on PB but not MB, would be expected to be more conducive to dissimilatory reduction of Mn and Fe in the sediments. Indeed, bottom concentrations of dissolved Mn were generally higher over PB than MB (Hatta et al., this issue). Further, bottom water concentrations of dissolved Fe over the western flank of PB were higher when the tidal flow was in the offshore direction, pointing to benthic sources of dissolved Fe from silty sediments further inshore (Figure 1). Based on sediment characteristics, PB would be expected to have stronger benthic sources of dissolved Fe.

Perhaps even more important than the differences in benthic sources of iron over the two banks are the distinct water column structures set up by the tidal contrasts. MB, unlike PB, had a more persistent and well-mixed bottom layer (Figure 6). Over all stations a homogeneous bottom layer was observed below a relatively sharp pycnocline at approximately 150m, well below the shallower MLs over PB. This more pronounced bottom mixed layer over MB likely inhibits the vertical flux of micronutrients from the lower layer to the euphotic zone. In contrast, the strongest density gradient over PB was at the shallower MLD within the upper 50m, and the bottom layer was characterized with a more gradual density gradient. The water column density structure over PB was thus more conducive for allowing bottom sources of micronutrients to mix further up into the water column and support primary production.

At MB, we observed deeper and more dynamic mixed layers. The light available to populations over each bank is dependent on the depth and consistency of these MLs and the attenuation of light through the surface layer. The higher biomass observed over PB attenuated light such that the median light levels over both banks were comparable.

The deeper more defined bottom layer observed over MB potentially resulted in lower vertical fluxes of iron into the euphotic zone. Lower photosynthetic efficiency (reduced ϕ, α_B and α) over MB is consistent with reduced Fe fluxes relative to PB. These lower photosynthetic efficiencies are thought to be due to over-production of photosynthetic pigments when phytoplankton are iron stressed; these excess pigments do not contribute to light harvesting (Behrenfeld and Milligan, 2013). Hiscock et al. (2008) similarly relate changes in ϕ and α_B to large changes in Fe availability measured during the Southern Ocean iron enrichment experiment.

The deeper and more dynamic mixed layers at MB may be expected to increase *P. antarctica* dominance, while the expected impact of potential differences in iron supply are less clear, as discussed above. Regardless, analysis of community composition from the two banks showed no clear differences in *P. antarctica* biomass; it was low on both banks and only had an relatively appreciable relative abundance in waters recently advected to the Ross Sea shelf from offshore (station 14 and Joides Basin; Figure 8 and Kohut et al., 2013). The most striking difference between the community composition at central PB (station 7) and MB was the dominance of the *Chaetoceros*-like clade at the latter location; this clade made only a modest (~10-15%) contribution to the other communities. The identity or particular physiological characteristics of this clade are unknown, but it is intriguing to speculate that this *Chaeotoceros*-like clade is more dominant due to an enhanced ability to flourish under low Fe. However, community composition analysis from complementary incubation experiments did not show any decreases in the relative abundance of this clade in response to Fe addition (Kustka et al. 2015b). Over the central PB, repeat sampling (Station 7 and 64, see Fig. 2b) revealed elevated areal and biomass normalized productivity and also was the only sites where *Phaeocystis* comprised less than 1% of the total 18S copy numbers. Additionally, the high relative abundances of two *Chaetoceros* spp. clades (not to be confused with the *Chaetoceros*-like clade) at PB stations 7 and 48 (combined abundances of 55% and 29%, respectively) starkly contrasted with those at station 70 (3.2% combined abundance), which may suggest a greater susceptibility to lower Fe fluxes for members of these clades.

Based on underway Fv/Fm measurements, both MB and PB populations appear to be growth rate limited by iron availability; this was corroborated by incubation experiments with PB populations (Kustka et al. 2015a). The dissolved Fe profiles were comparable on both banks (Figure 7) with notably similar surface water drawdowns of dissolved Fe relative to concentrations at depth. The elevated biomass and productivity on PB compared to MB suggests the vertical flux of iron to the surface waters on MB may have been impeded. This is supported by the fundamental differences in the physical structure of the water columns at the two banks, as discussed above.

5. Conclusions

The summer bloom over the Northern Ross sea exhibits a persistent spatial distribution with higher biomass over PB compared to MB. Differences in the strength of the tides driven by the local topography of each bank are likely to influence the availability of iron and light to the phytoplankton communities in the waters above. Stronger tides over MB scour the seafloor inhibiting the availability of sedimentary sources of Fe. In the water column, the stronger tides mix the surface layer leading to deeper, less defined MLDs that potentially limit the vertical flux of deep Fe to those populations compared to the more stable and shallow MLDs observed over PB. Overall the conditions observed over and around PB were more conducive to support the increased biomass observed through the years over this bathymetric feature. The water column stability and proximity of silty sediments maintained by weaker currents likely support this higher biomass observed over central PB.

Acknowledgements

The NSF Office of Polar Programs supported the Slocum Enhanced Adaptive Fe Algal Research in the Ross Sea (SEAFAReRS) project (ANT-0839039). We would also like to thank the entire crew of the *RVIB Nathaniel B. Palmer* for their support throughout the cruise and the Raytheon Polar Services personnel for logistical assistance. In addition, we are grateful to John Kerfoot (Rutgers) for the glider processing before and after the deployment.

References

Anderson, J.B., Brake, C.F., Myers, N.C., 1984. Sedimentation on the Ross Sea continental shelf, Antarctica. Marine Geology 57 (1–4), 295-333. 10.1016/0025-3227(84)90203-2.

Arrigo, K. R., and G. L. Van Dijken. 2004. Annual changes in sea-ice, chlorophyll a, and primary production in the Ross Sea, Antarctica. Deep. Res. Part II Top. Stud. Oceanogr. **51**: 117–138.

Arrigo, K.R. and McClain, C.R., 1994. Spring phytoplankton production in the western Ross Sea. Science: 266: 261-263

Arrigo, K.R., Robinson, D.H., Worthen, D.L., Dunbar, R.B., DiTullio, G.R., VanWoert, M., Lizotte, M.P., 1999. Phytoplankton community structure and the drawdown of nutrients and CO2 in the Southern Ocean. Science 283 (5400), 365-367.

Arrigo, K. R., G. L. van Dijken, and S. Bushinsky. 2008a. Primary production in the Southern Ocean, 1997-2006. J. Geophys. Res. Ocean. **113**: 1997–2006.

Arrigo, K.R., G.L. van Dijken, and M. Long. 2008b. Coastal Southern Ocean: A strong anthropogenic CO2 sink. Geophys. Res. Letters. 35: L21602.

Asper, V., and W. O. Smith Jr. 1999. Particle fluxes during austral spring and summer in southern Ross Sea, Antarctica, J. Geophys. Res., 104, 5345– 5359.

Ballard G, Jongsomjit D, Veloz SD, Ainley DG (2012) Coexistence of mesopredators in an 576 intact polar ocean ecosystem: The basis for defining a Ross Sea marine protected area. Biol 577 Conserv 156:72-82

Behrenfeld, M. J. and Milligan, A. J. (2013) Photophysiological Expressions of Iron Stress in Phytoplankton. Annu. Rev. Mar. Sci., 5, 217-246.

Berger, C.J.M., Lippiatt, S.M., Lawrence, M.G., Bruland, K.W., 2008. Application of a chemical leach technique for estimating labile particulate aluminum, iron, and manganese in the Columbia River plume and coastal waters off Oregon and Washington. J. Geophys. Res. 113, C00B01. 10.1029/2007jc004703.

Bertrand, E. M., M.A. Saito, J. M. Rose, C.R. Riesselman, M.C. Lohan, 2007. A.E. Noble, P.A. Lee, and G.R. DiTullio, Vitamin B12 and iron colimitation of phytoplankton growth in the Ross Sea., Limnol. Oceanogra. , 52, 1079-1093, doi:10.4319/lo.2007.52.3.1079.

Carvalho, F., Schofield, O., Oliver, M., Kohut, J. 2016. Mixing and phytoplankton dynamics in Antarctica's Coastal Seas. (In Prep).

Cetinić, I., Perry, M.J., Briggs, N.T., Kallin, E., D'Asaro, E.A., Lee, C.M., 2012.Particulate organic carbon and inherent optical properties during 2008 North Atlantic bloom experiment.J.Geophys.Res.Ocean117.

Coale, K. H., X. J. Wang, S. J. Tanner, and K. S. Johnson. 2003. Phytoplankton growth and biological response to iron and zinc addition in the Ross Sea and Antarctic Circumpolar Current along 170°W. Deep Sea Research Part II 50:635–653, doi:10.1016/ S0967-0645(02)00588-X.

Cotté C, Simard Y. 2005. Formation of dense krill patches under tidal forcing at whale feeding hot spots in the St. Lawrence Estuary. *Marine Ecology Progress Series* 288: 199–210. doi: 10.3354/meps288199.

Dinniman, M. S., Klinck, J. M., & Smith, W. O. 2003. Cross-shelf exchange in a model of the Ross Sea circulation and biogeochemistry. Deep Sea Research Part II: Topical Studies in Oceanography, 50(22-26), 3103-3120. doi: 10.1016/j.dsr2.2003.07.011

Erofeeva, S. Y., L. Padman and G. Egbert. 2005. Assimilation of Ship-Mounted ADCP Data for Barotropic Tides: Application to the Ross Sea. Journal of Atmospheric and Oceanic Technology 22(6): 721-734.

Gardner, W.D., Mishonov, A.V., Richardson, M.J., 2006.Global POC concentrations from in-situ and satellite data. DeepSeaRes. PartII Top.Stud.Oceanogr.53, 718–740.

Gordon, A. L., L. Padman and A. Bergamasco. 2009. Southern Ocean shelf slope exchange. Deep Sea Research Part II: Topical Studies in Oceanography 56(13-14): 775-777.

Halsey, K.H., Milligan, A.J., and Behrenfeld, M.J. 2011. Linking time-dependent carbon fixation efficiencies in Dunaliella tertiolecta (Chlorophyceae) to underlying metabolic pathways. J. Phycol. 47:66-76.

Hatta et al., this volume The relative roles of Modified Circumpolar Deep Water and sediment resuspension in maintaining the phytoplankton blooms above Pennell and Mawson Bank, Ross Sea.

Hiscock, M.R., Lance, V.P., Apprill, A., Bidigare, Johnson, Z.I., R.R., Mitchell, B.G., Smith, Jr., W. O., Barber, R.T., 2008. Photosynthetic maximum quantum yield increases are an essential component of the Southern Ocean phytoplankton response to iron. Proceedings of the National Academy of Science, 105, 4775-4780.

Hunt Jr G. L., Russell R. W., Coyle K. O., Weingartner T. 1998. Comparative foraging ecology of planktivorous auklets in relation to ocean physics and prey availability. *Marine Ecology Progress Series* 167: 241–259. doi: 10.3354/meps167241

Jones, B.M., and Kustka, A.B. (Submitted) Quantitative SMRT cell sequencing unveils differential distribution of protists in the Ross Sea, Antarctica. *Marine Biotechnology*

Kishino, M., Takahashi, M., Okami, N., Ichimura, S., 1985. Estimation of the spectral absorption coefficients of phytoplankton in the sea. Bull. Mar. Sci. 37 (2), 634-642.

Kohut, J., Hunter, E., Huber, B., 2013. Small-scale variability of the cross-shelf flow over the outer shelf of the Ross Sea. Journal of Geophysical Research: Oceans 118 (4), 1863-1876. 10.1002/jgrc.20090.

Kropuenske, L.R.,Mills,M.M.,VanDijken,G.L.,Bailey,S.,Robinson,D.H.,Welsch- meyer, N.A.,Arrigo,K.R. 2009. Photophysiology in two major Southern Ocean phytoplankton taxa: photoprotectionin Phaeocystis antarctica and Fragilar-iopsis cylindrus. Limnol.Oceanogr. 54(4),1176–1196.

Kustka, A., Jones, B.M., Hatta, M., Field, M. P., and A. J. Milligan, 2015a. The influence of iron and siderophores on eukaryotic phytoplankton growth rates and community composition in the Ross Sea, Marine Chemistry. 173. 195-207. doi:10.1016/j.marchem.2014.12.002.

Kustka, A.B., J.T. Kohut, A. White, P.J. Lam, A. Milligan, M. Dinniman, S. Mack, M. Hiscock, E. Hunter, W.O. Smith, Jr., and C.I. Measures. 2015b. The role of Modified Circumpolar Deep Water as an iron source to productive mid-summer phytoplankton in the Ross Sea. Deep Sea Res. 105:171-185.

Lee, K., Tong, L.T., Millero, F.J., Sabine, C.L., Dickson, A.G., Goyet, C., Park, G.-H., Wanninkhof, R., Feely, R.A., Key, R.M., 2006. Global relationships of total alkalinity with salinity and temperature in surface waters of the world's oceans. Geophys.Res.Lett.33, L19605.

Lorbacher, K., D. Dommenget, P. Niiler, and A. Köhl. 2006. Ocean mixed layer depth: A subsurface proxy of ocean-atmosphere variability, Journal of Geophysical Research: Oceans (1978–2012), 111(C7).

Martin, J.H., R.M. Gordon, and S.E. Fitzwater. 1991. The case for iron, Limnol. Oceanography 36(8), 1793-1802.

Measures, C. I., W. M. Landing, M. T. Brown, and C. S. Buck. 2008. A commercially a vailable rosette system for trace metal clean sampling, *Limnol. Oceanogr. Methods* 6:384-394. doi: 10.4319/lom.2008.6.384.

Measures, C.I., J. Yang, and J.A. Resing, J. 1995. Determination of iron in seawater by flow injection analysis using in-line preconcention and spectrophotometric detection, Mar. Chem., 50, 3-12, 1995.

Milne, A., Landing, W., Bizimis, M., Morton, P. 2010. Determination of Mn, Fe, Co, Ni, Cu, Zn, Cd and Pb in seawater using high resolution magnetic sector inductively coupled mass spectrometry (HR-ICP-MS). Anal. Chim. Acta. 665, 200–207.

Mitchell, B.G., 1990. Algorithms for determining the absorption coefficient of aquatic particulates using the Quantitative Filter Technique (QFT). Society of Photo-Optical Instrumentation Engineers 10, 137-148.

Ohnemus, D.C., Auro, M.E., Sherrell, R.M., Lagerstrom, M., Morton, P.L., Twining, B.S., Rauschenberg, S., Lam, P.J., 2014. Laboratory intercomparison of marine particulate digestions including Piranha: a novel chemical method for dissolution of polyethersulfone filters. Limnology and Oceanography-Methods 12, 530-547. 10.4319/lom.2014.12.530.

Ohnemus, D.C., Lam, P.J., 2015. Cycling of lithogenic marine particles in the US GEOTRACES North Atlantic transect. Deep Sea Research Part II: Topical Studies in Oceanography 116, 283-302. http://dx.doi.org/10.1016/j.dsr2.2014.11.019.

Orsi, A. H. and C. L. Wiederwohl (2009). A recount of Ross Sea waters. Deep Sea Research Part II: Topical Studies in Oceanography. 56(13-14): 778-795.

Padman, L., Howard, S., Orsi, A., Muench, R., 2009. Tides of the Northwestern Ross Sea and their impact on dense outflows of high salinity shelf water. In: Gordon, A., Padman, L., Bergamasco, A. (Eds.), Deep-Sea Research AnSlope/Clima topical volume. Southern Ocean Shelf Slope Exchange.

Raiswell, R., Canfield, D.E., Berner, R.A., 1994. A comparison of iron extraction methods for the determination of degree of pyritisation and the recognition of iron-limited pyrite formation. Chemical Geology 111 (1-4), 101-110.

Robertson, R. 2005. Baroclinic and barotropic tides in the Ross Sea. Antarctic Science, 17(1), 107-120. doi: 10.1017/s0954102005002506

Schofield, O., Kohut, J., Aragon , D., Creed, L., Graver, J., Haldeman, C., Kerfoot, J., Roarty, H., Jones, C., Webb, D., Glenn, S. M (2007). Slocum Gliders: Robust and ready. Journal of Field Robotics, 24(6): 1-14, doi: 10:1009/rob.20200.

Sedwick, P.N., DiTullio, G.R., Mackey, D.J., 2000. Iron and manganese in the Ross Sea, Antarctica: Seasonal iron limitation in Antarctic shelf waters. Journal of Geophysical Research-Oceans 105 (C5), 11321-11336.

Sedwick, P. N., C.M. Marsay, B.M. Sohst, A.M. Aguilar-Islas, M.C. Lohan, M.C. Long, K.R. Arrigo, R.B. Dunbar, M.A. Saito, W.O. Smith, G.R. DiTullio, 2011. Early season depletion of dissolved iron in the Ross Sea polynya: Implications for iron dynamics on the Antarctic continental shelf, J. Geophys. Res., 116, C12019, doi:10.1029/2010JC006553.

Slade, W.H., Boss, E., Dall'olmo, G., Langner, M.R., Loftin, J., Behrenfeld, M.J., Roesler, C., Westberry, T.K., 2010. Underway and moored methods for improving accuracy in measurement of spectral particulate absorption and attenuation. J. Atmos. Ocean. Technol. 27, 1733–1746.

Smith, W.O., Comiso, J.C., 2008. Influence of sea ice on primary production in the Southern Ocean: a satellite perspective. J.Geophys.Res.113,1–19.

Smith, W.O., David G. Ainley, Kevin R. Arrigo, and Michael S. Dinniman. 2014. The Oceanography and Ecology of the Ross Sea. Annu. Rev. Mar. Sci. 6:469–87

Strickland, J.D.H., and Parsons, T.R. 1972. A practical handbook of seawater analysis. Fisheries Res. Board of Canada, Ottowa, 310 pp.

Sunda, W.G. and S. Huntsman. 1997. Interrelated influence of iron, light and cell size on marine phytoplankton growth. Nature 390:389-392.

Vink, S., E.A. Boyle, C.I. Measures and J. Yuan. 2000. Automated high resolution determination of the trace elements iron and aluminium in the surface ocean using a towed fish coupled to flow injection analysis, Deep-Sea Research, 47, 1141-1156.

Vlietstra L. S., Coyle K. O., Kachel N. B., Hunt Jr G. L. 2005 Tidal front affects the size of prey used by a top marine predator, the short-tailed shearwater (*Puffinus tenuirostris*). *Fisheries Oceanography* 14: 196–211. doi: 10.1111/j.1365-2419.2005.00369.x

Wentworth, C.K., 1922. A scale of grade and class terms for clastic sediments. The Journal of Geology, 377-392.

Whitworth, T. and A. H. Orsi (2006). Antarctic Bottom Water production and export by tides in the Ross Sea. Geophysical Research Letters. 33(12).

Zhu, F., R. Massana, F. Not, D. Marie, And D. Vaulot. 2005. Mapping Of Picoeucaryotes In Marine Ecosystems With Quantitative PCR Of The 18s Rrna Gene. Fems Microbiology Ecology 52: 79-92.

List of Tables and Figures

Table 1: Surface sediment grain size classification (volume %). Station abbreviations are Mawson Bank West (MW), Central Mawson Bank (MT), Mawson Bank East (ME), Joides Basin (JB), Pennell Bank West (PW), Central Pennell Bank (PT), and Pennell Bank East (PE). *Wentworth sediment classes are defined as: silty sand=sand>silt>10%; sandy silt=silt>sand>10%; clayey silt=silt>clay>10% (Wentworth, 1922). All other classes <10%.

Table 2. Underway variable fluorescence from select stations. Average values from 60 observations (within 30 minutes preceding and following station arrival time) are reported. Locations refer to Central Pennell Bank and Mawson Bank, respectively. Time of sampling is listed as Julian day relative to GMT. Irradiance (mast PAR) is expressed in umol photon m^{-2} s^{-1}. Fv/Fm was measured using a Satlantic FIRE fluorometer as described in text. For calculations of location Fv/Fm, observations where mast PAR exceeded 300 μmol photon m^{-2} s^{-1} were omitted (corresponding to ~ 100 μmol photon m^{-2} s^{-1} at the collection depth) due to potential non-photochemical quenching.

Table 3. Primary productivity rates as well as parameters of hyperbolic tangent model for 24-hr 14C incubations. Error terms are the confidence intervals of the model fit. Maximal productivity rates are shown as calculated with and without normalization to chlorophyll. The quantum yield is calculated as denoted in the text; the half saturation coefficient (Ek) is determined from Pmax and alpha. The location of each station relative to the longitudinal bank topography is noted as EF (Eastern Flank), CB (Central Basin), or WF (Western Flank).

Figure 1. Map of the study site in the Western Ross Sea showing the ship track (black line), ship stations (black dots), and glider tracks (green). Isobaths highlight the relevant topographic features including Ross Bank (RB), Pennell Bank (PB), Joides Basin (JB), and Mawson Bank (MB). The colored circles indicate the broad sediment characteristics of surface sediments.

Figure 2. Historical and 2011 mid-summer biomass proxies across transect spanning Pennell and Mawson Banks. a) MODIS-derived Chl a concentration (ug/L) during our survey in January/February 20112011. Our primary sampling transect across the banks is shown in red. b) Underway estimates of particulate organic carbon from hyperspectral absorbance and attenuation. c) January through February mean satellite derived Chl a concentration along our sampling line from 1998-2014. d) Sample mean Chl a concentration along the same transect with underlying bathymetry.

Figure 3. Velocity characteristics across transect spanning PB and MB a) detided depth averaged currents (black vectors) and surface temperature (colored track). The depth dependent velocity sections (m/s) for the cross bank (b) and along bank (c) velocity components. These are the average of cross-sections sampled between Jan 22 and Feb 12, 2011.

Figure 4. Average cross section of potential temperature (°C, top), salinity (psu, middle) and dissolved oxygen (ml L^{-1}, bottom). The stations sampled as part of the across bank section are shown as vertical dashed lines. The neutral density bounds defining MCDW (28.00-28.27 kg m^{-3}) are shown in black and the topographic features are labeled as in Figure 1.

Figure 5. Glider cross-sections of Temperature (top row) and Chlorophyll Concentration determined from fluorescence (bottom Row). The deployment over PB is the right column and the deployment over MB is the left column. The direction the glider was travelling relative to the slope (Deeper) and peak (Shallower) of each bank is indicated below. The tracks are shown as green lines in Figure 1.

Figure 6: Shipboard profiles of Density (dashed blue) and Chl a Fluorescence (green) for the central PB (upper row) and MB (lower row) Stations. The estimated MLD is shown as a solid red line for each station. The date, station number, MLD and quality index (QI) are indicated for each profile. The average MLD and MLD integrated Chl a fluorescence for each bank is also shown.

Figure 7: The vertical depth (m) profiles of (a) dissolved Fe (dFe, nM) and (b) leachable particulate Fe (pFe, nM) for the repeated stations above PB (Stations 7-red circles and 61-green squares) and above MB (Station 70-purple diamonds).

Figure 8. Relative abundances of 18S rDNA from phytoplankton genera at PB (7), off the shelf (14), PB West (24), PB North (48) and MB (70). Operationally defined taxonomic units (OTUs) were clustered at 98% sequence similarity. For clarity, only OTUs representing at least 1% of phototroph OTUs are shown, so some treatments have summed relative abundances less than 100%. For station 7 (PB), the relative abundances of four relatively rare diatom OTUs (with similarity to *Proboscia* spp., *Thalassiosira* spp., *Thalassiothrix* spp., and *Pleurosigma* spp.) are pooled as, “four other diatom clades”. Assemblage data were derived from single samples collected from the mixed layer at each station.

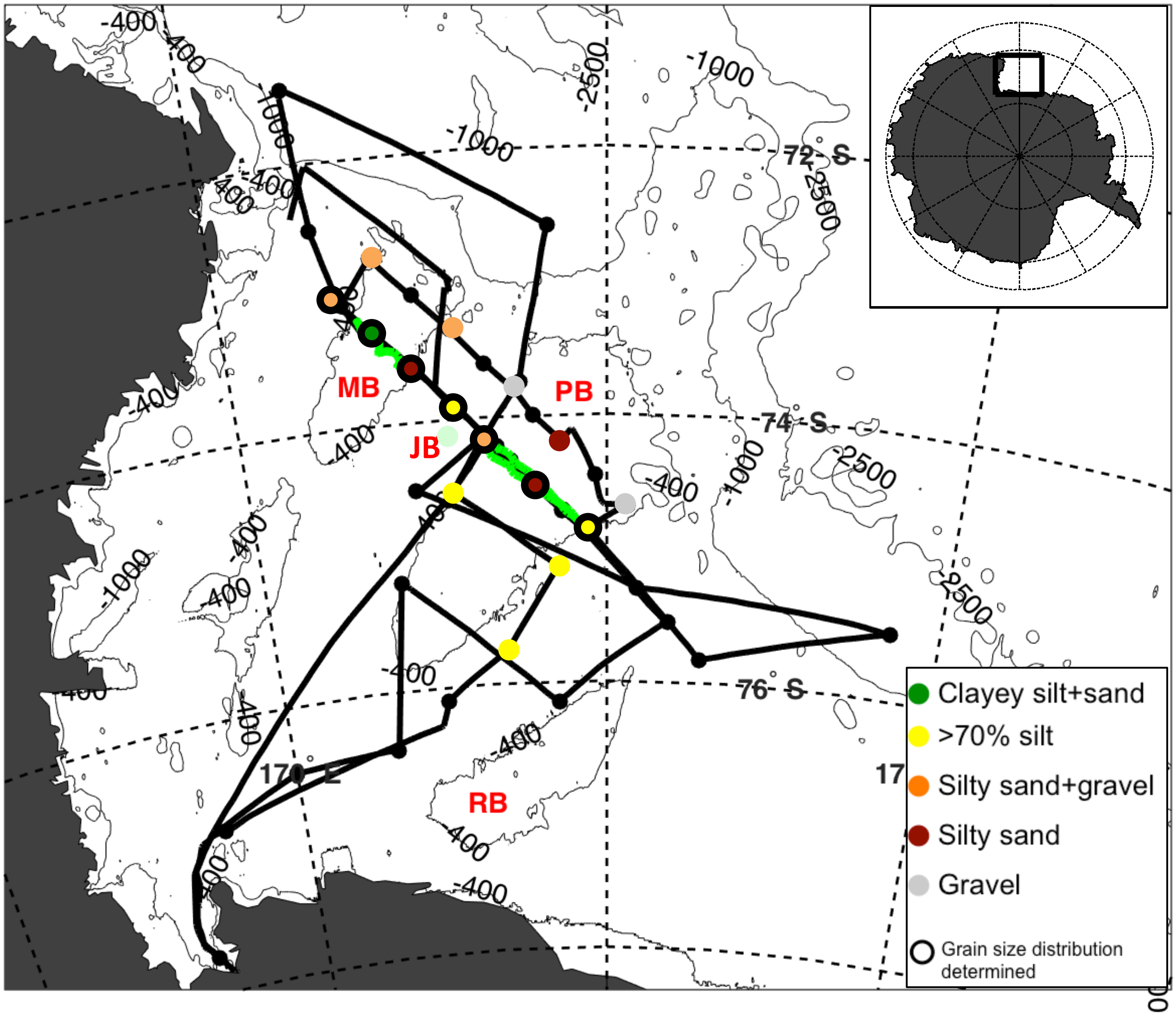

Figure 1. Map of the study site in the Western Ross Sea showing the ship track (black line), ship stations (black dots), and glider tracks (green). Isobaths highlight the relevant topographic features including Ross Bank (RB), Pennell Bank (PB), Joides Basin (JB), and Mawson Bank (MB). The colored circles indicate the broad sediment characteristics of surface sediments.

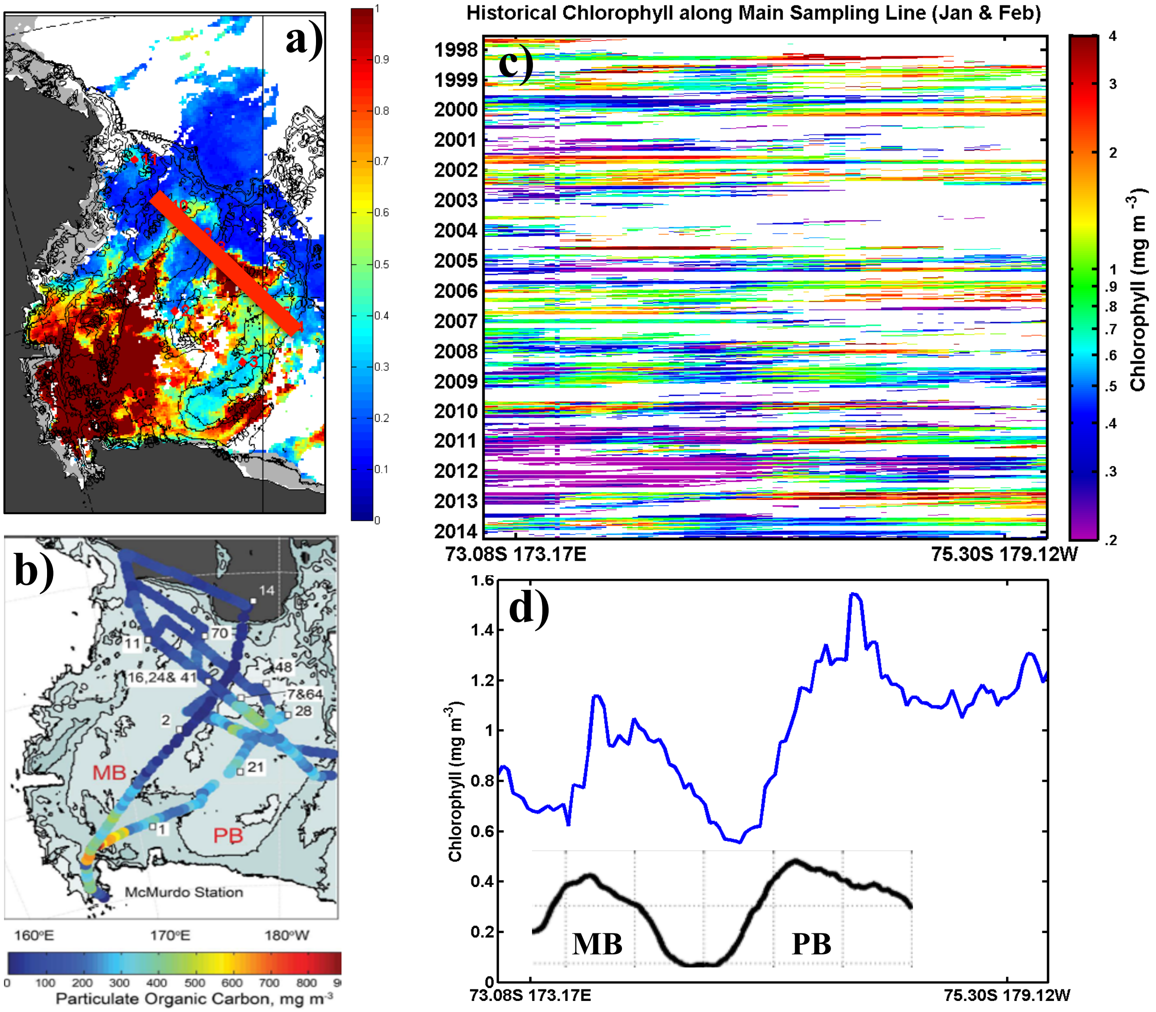

Figure 2. Historical and 2011 mid-summer biomass proxies across transect spanning Pennell and Mawson Banks. a) MODIS-derived Chl a concentration (ug/L) during our survey in January/February 20112011. Our primary sampling transect across the banks is shown in red. (B) Underway estimates of the concentration of surface POC; station locations where photosynthetic rates are noted as text. c) January through February mean satellite derived Chl a concentration along our sampling line from 1998-2014. d) Sample mean Chl a concentration along the same transect with underlying bathymetry.

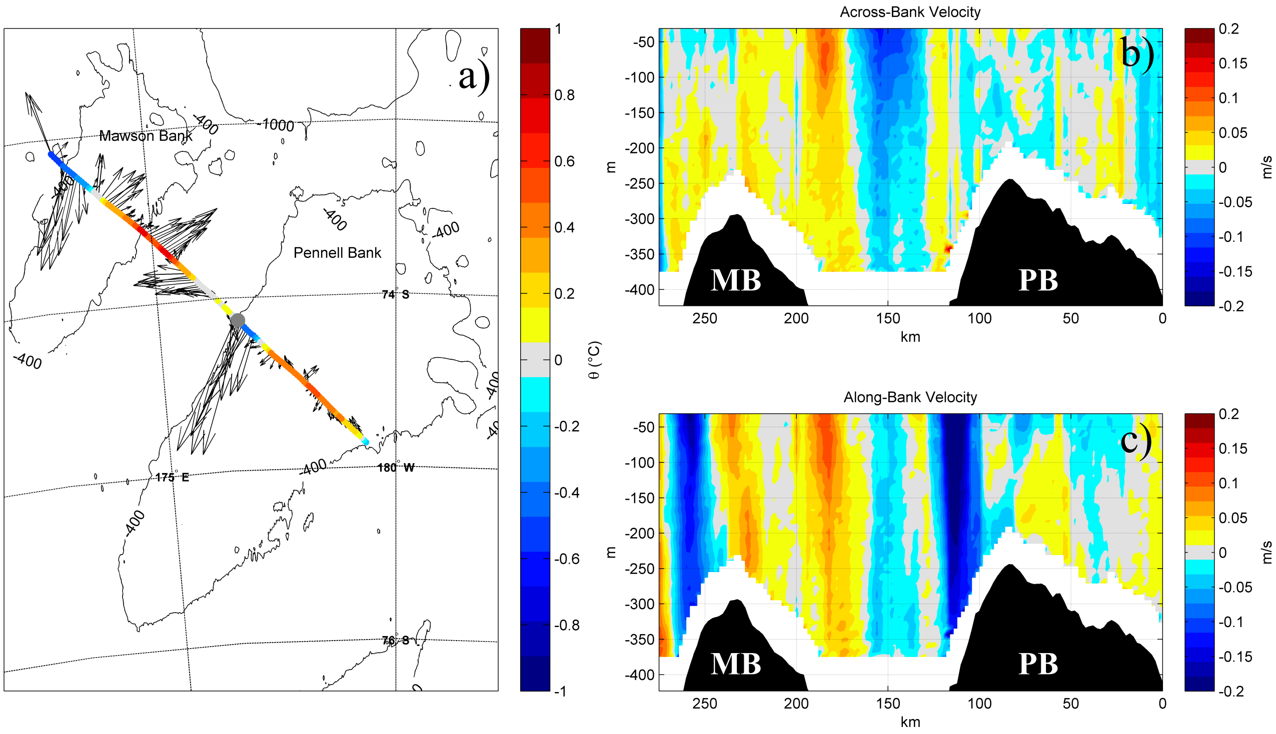

Figure 3. Velocity characteristics across transect spanning PB and MB a) detided depth averaged currents (black vectors) and surface temperature (colored track). The depth dependent velocity sections (m/s) for the cross bank (b) and along bank (c) velocity components. These are the average of cross-sections sampled between Jan 22 and Feb 12, 2011.

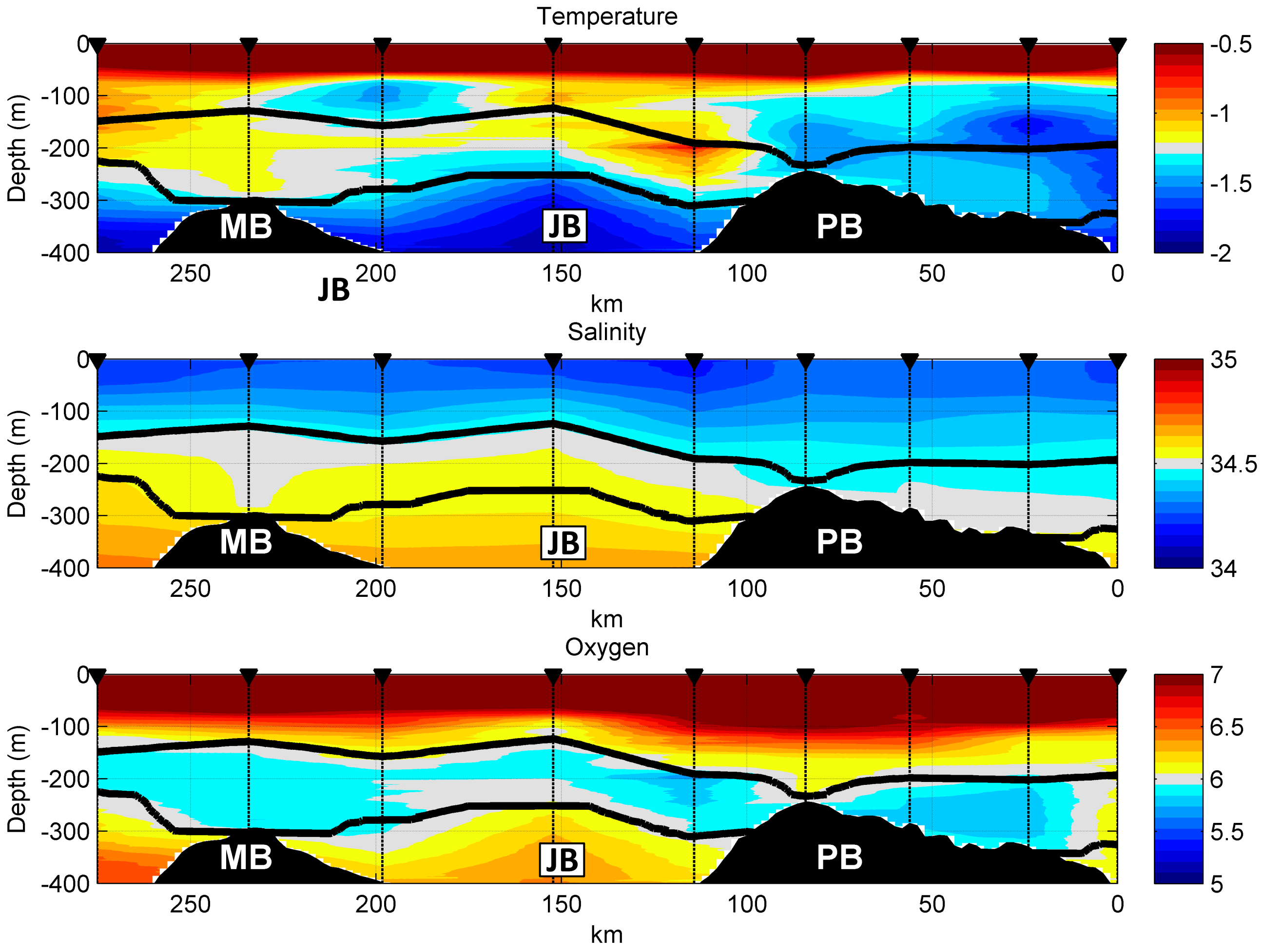

Figure 4. Average cross section of potential temperature (°C, top), salinity (psu, middle) and dissolved oxygen (ml L^{-1}, bottom). The stations sampled as part of the across bank section are shown as vertical dashed lines. The neutral density bounds defining MCDW (28.00-28.27 kg m^{-3}) are shown in black and the topographic features are labeled as in Figure 1.

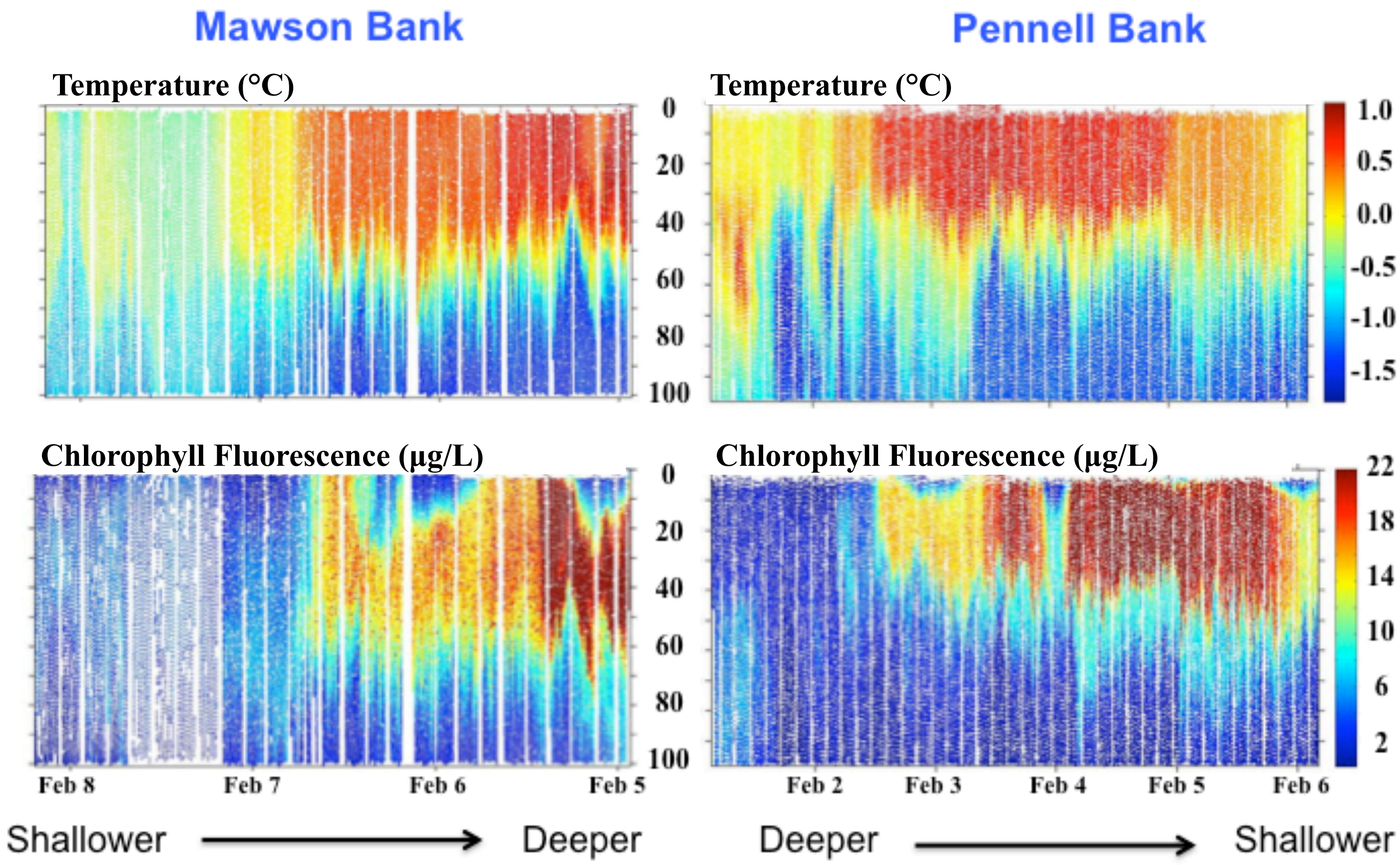

Figure 5. Glider cross-sections of Temperature (top row) and Chlorophyll Concentration determined from fluorescence (bottom Row). The deployment over PB is the right column and the deployment over MB is the left column. The direction the glider was travelling relative to the slope (Deeper) and peak (Shallower) of each bank is indicated below. The tracks are shown as green lines in Figure 1.

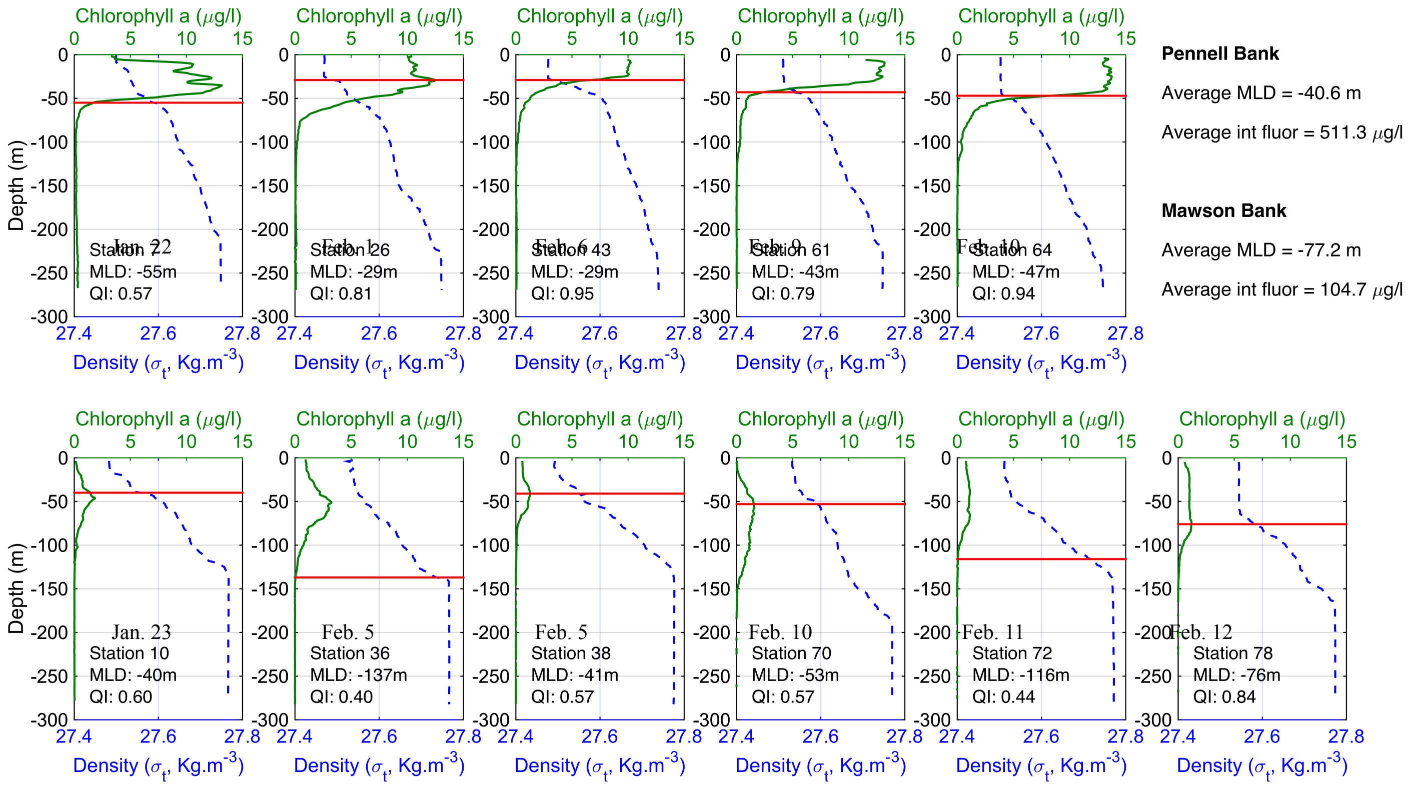

Figure 6: Shipboard profiles of Density (dashed blue) and Chl a Fluorescence (green) for the central PB (upper row) and MB (lower row) Stations. The estimated MLD is shown as a solid red line for each station. The date, station number, MLD and quality index (QI) are indicated for each profile. The average MLD and MLD integrated Chl a fluorescence for each bank is also shown.

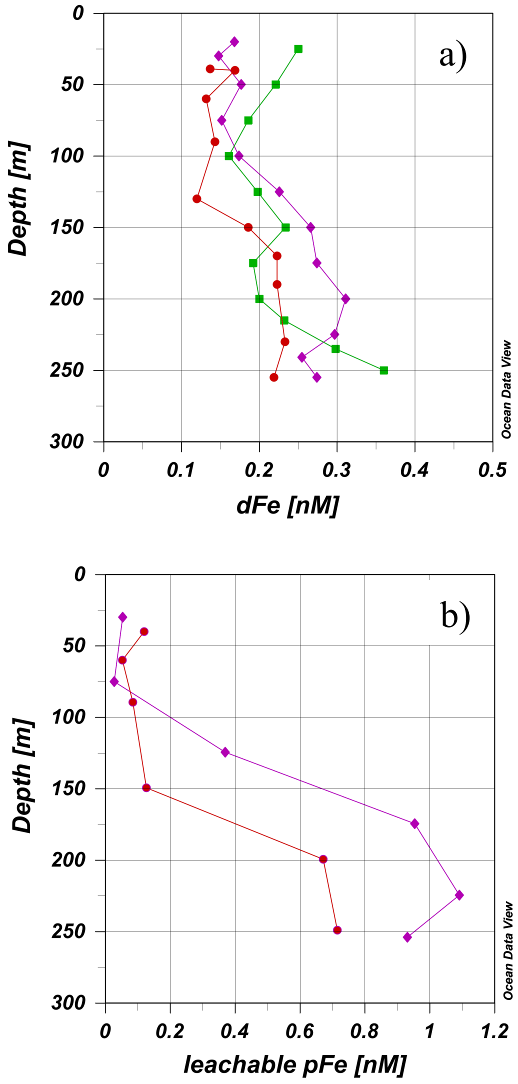

Figure 7: The vertical depth (m) profiles of (a) dissolved Fe (dFe, nM) and (b) leachable particulate Fe (pFe, nM) for the repeated stations above PB (Stations 7-red circles and 61-green squares) and above MB (Station 70-purple diamonds).

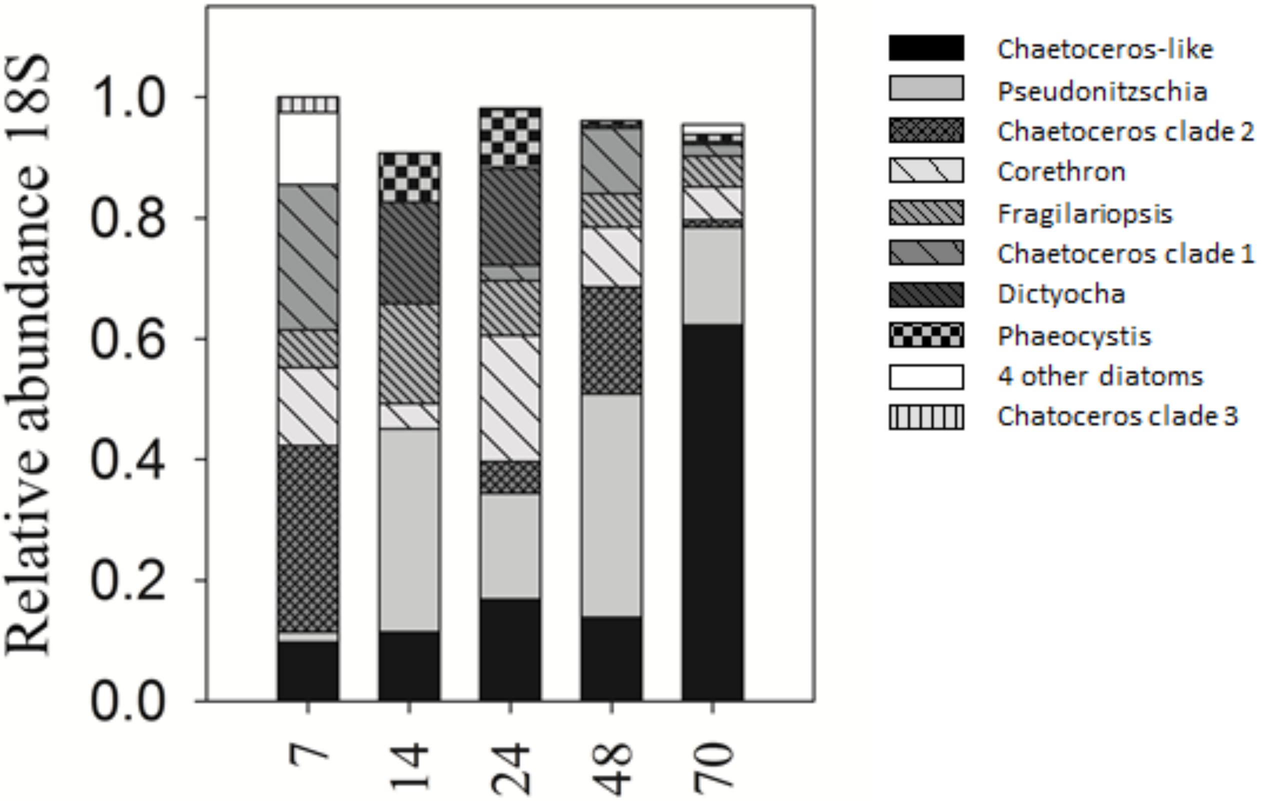

Figure 8. Relative abundances of 18S rDNA from phytoplankton genera at PB (7), off the shelf (14), PB West (24), PB North (48) and MB (70). Operationally defined taxonomic units (OTUs) were clustered at 98% sequence similarity. For clarity, only OTUs representing at least 1% of phototroph OTUs are shown, so some treatments have summed relative abundances less than 100%. For station 7 (PB), the relative abundances of four relatively rare diatom OTUs (with similarity to *Proboscia* spp., *Thalassiosira* spp., *Thalassiothrix* spp., and *Pleurosigma* spp.) are pooled as, “four other diatom clades”. Assemblage data were derived from single samples collected from the mixed layer at each station.

Table 1: Surface sediment grain size classification (volume %)

Station#	71-MW	70-MT	35-ME	34-JB	41-PW	26-PT	28-PE
Clay: <4um	5	27	3	13	3	2	9
Silt: 4-63um	22	53	12	79	12	14	73
sand: 63um-2mm	73	20	85	8	86	84	17
Wentworth sediment class*	silty sand +gravel	clayey silt +sand (>10%)	silty sand	clayey silt	silty sand +gravel	silty sand	sandy silt

Station abbreviations are Mawson Bank West (MW), Central Mawson Bank (MT), Mawson Bank East (ME), Joides Basin (JB), Pennell Bank West (PW), Central Pennell Bank (PT), and Pennell Bank East (PE)

*Wentworth sediment classes are defined as: silty sand=sand>silt>10%; sandy silt=silt>sand>10%; clayey silt=silt>clay>10% (Wentworth, 1922). All other classes <10%.

Table 2. Underway variable fluorescence from select stations.

Station	Location	Julian day (GMT)	PAR	Fv/Fm (sd)
26	Central PB	32.50	30	0.247 (0.014)
43	Central PB	37.57	13	0.285 (0.017)
61	Central PB	40.92	891	0.277 (0.017)
64	Central PB	41.28	584	0.265 (0.022)
36	Central MB	36.42	42	0.313 (0.016)
38	Central MB	36.66	48	0.315 (0.029)
70	Central MB	41.96	1593	0.191 (0.021)
72	Central MB	42.56	5	0.281 (0.034)
78	Central MB	43.86	298	0.267 (0.036)

Average values from 60 observations (within 30 minutes preceding and following station arrival time) are reported. Locations refer to Central Pennell Bank and Mawson Bank, respectively. Time of sampling is listed as Julian day relative to GMT. Irradiance (mast PAR) is expressed in umol photon m^{-2} s^{-1}. Fv/Fm was measured using a Satlantic FIRE fluorometer as described in text. For calculations of location Fv/Fm, observations where mast PAR exceeded 300 μmol photon m^{-2} s^{-1} were omitted (corresponding to ~ 100 μmol photon m^{-2} s^{-1} at the collection depth) due to potential non-photochemical quenching.

Table 3. Primary productivity rates as well as parameters of hyperbolic tangent model for 24-hr 14C incubations.

Date (2011)	Station	**Mixed Layer Integrated NPP** g C m^{-2} d^{-1}	$\mathbf{P_{max}}$ mg C m^{-3} d^{-1}	**a**, mg C m^{-3} d^{-1} mmol photons m^{-2} s^{-1}	$\mathbf{P_b^{max}}$ g C g chl^{-1} h^{-1}	**Quantum Yield** mol C mol photons $^{-1}$	$\mathbf{E_k}$ µmol m^{-2} s^{-1}
Mawson Bank							
24-Jan	11, EF	1.14	38 ± 3	0.4 ± 0.1	4.3 ± 0.4	0.013 ± 0.003	93.2
11-Feb	70, C	0.60	12 ± 2.7	0.7 ± 0.4	1.6 ± 0.3	0.022 ± 0.013	17.4
Clivar S4P (Located near the EF of Pennell Bank)							
27-Jan	16	0.76	15 ± 1	0.3 ± 0.1	1.8 ± 0.1	0.018 ± 0.004	47.7
1-Feb	24	0.34	17 ± 2	0.5 ± 0.2	1.5 ± 0.2	0.019 ± 0.007	36.3
6-Feb	41	0.78	26 ± 3	0.5 ± 0.2	1.6 ± 0.1	0.009 ± 0.003	46.7
Pennell Bank							
21-Jan	02, EF	0.57	34 ± 2	0.3 ± 0.1	8.4 ± 0.6	0.009 ± 0.001	127.9
23-Jan	07, CB	2.36	167 ± 16	4.0 ± 1.1	4.2 ± 0.4	0.069 ± 0.019	41.9
31-Jan	21, WF	5.26	123 ± 14	4.2 ± 1.3	2.9 ± 0.8	0.094 ± 0.029	29.38
8-Feb	48, CB	1.04	45 ± 3	0.9 ± 0.2	1.8 ± 0.1	0.013 ± 0.003	49.74
10-Feb	64, CB	6.37	155 ± 14	5.5 ± 1.3	3.2 ± 0.3	0.060 ± 0.014	28.16

Error terms are the confidence intervals of the model fit. Maximal productivity rates are shown as calculated with and without normalization to chlorophyll. The quantum yield is calculated as denoted in the text; the half saturation coefficient (Ek) is determined from Pmax and alpha. The location of each station relative to the longitudinal bank topography is noted as EF (Eastern Flank), CB (Central Basin), or WF (Western Flank).